Halloysite nanotubes for regulating thermodynamics and kinetics of polysulfone/poly (ethylene-co-vinyl alcohol) copolymer mixed matrix membranes with enhanced antifouling, permeability, and mechanical strength

Jianxin Li（✉ jxli@tiangong.edu.cn ）

TIANGONG UNIVERSITY   https://orcid.org/0000-0002-4085-9720

Sania Kadanyo

Tiangong

Christine N Matindi

TIANGONG UNIVERSITY

Derrick Dlamini

University of California at Los Angeles

Yunxia Hu

Tiangong University

Zhenyu Cui

Tiangong University

Benqiao He

Tiangong University

Bhekie Mamba

University of South Africa

Nozipho Gumbi

University of South Africa   https://orcid.org/0000-0002-2479-7187

Abstract

In this study, hydrophilic halloysite nanotubes (HNTs) and poly (ethylene-co-vinyl alcohol) (EVOH) were mixed with hydrophobic polysulfone (PSF) in the presence of polyethylene glycol (PEG) to fabricate mixed matrix membranes (MMMs) free of macrovoids and enhanced performance via non-solvent induced phase separation (NIPS) technique. Various analytical techniques were used to probe the MMMs in terms of surface and cross-sectional morphology, functional groups, hydrophilicity, and mechanical strength. The separation and antifouling properties of PSF/EVOH/HNTs membranes were performed by bovine serum albumin (BSA) solution and gasoline (Oil) emulsion. The results showed delayed demixing and the formation of PSF/EVOH-MMMs with a spongy structure when the content of HNTs in the casting solutions was varied from 0.06–0.12 wt.%, owing to the formation of strong hydrogen bonds between PSF, EVOH, PEG and HNTs, which was confirmed by molecular dynamics (MD) simulations. The mechanical strength of the MMMs with 0.12 wt.% HNTs was increased 2.2-fold (up to 6.22 MPa), while the contact angle (CA) was the lowest at 47.42 ± 1.9°, indicating a significant increase in hydrophilicity. The underwater super oleophobic CA of the MMMs (169°) also showed a 21% improvement over the pristine membrane (137°). At the same time, the water permeability increased by a factor of 1.7 up to 419 $L\ m^{-2}\ h^{-1}\ bar^{-1}$ compared to the pristine membrane (0 wt.% HNTs) ($246\ L\ m^{-2}\ h^{-1}\ bar^{-1}$). The rejection rates of MMMs (M12) for oil and BSA were > 90% and > 95%, respectively. After three cycles of fouling and cleaning experiments, the MMMs had > 90% flux recovery for both oil and BSA. In conclusion, this study demonstrates a new way to control the dope thermodynamics, formation dynamics, as well as morphology of MMMs by using the synergy of HNTs and polymers while maintaining promising properties for an improved separation performance of the UF membrane.

Highlights

- The addition of HNTs altered the thermodynamics of PSF/EVOH dope due to H-bonding
- MD simulations and Raman data demonstrated H-bonding in the MMMs
- HNTs induced delayed demixing and gave MMMs a fully spongy structure
- HNTs adding enhanced the mechanical and thermal properties of MMMs due to H-bonding
- MMMs showed markedly improved hydrophilicity, permeance, and antifouling properties

Introduction

Water consumption is increasing at a rate that is twice that of the population growth[1]. Water scarcity is expected to affect more than 2 billion people by 2050 due to the pressing issues of the continuing increase in population, climate change, and increased urbanization[12]. Wastewater reclamation and recycling have received attention as reliable strategies for addressing the water scarcity issue. There exist numerous industrial effluents. Among them, oily water and protein wastewater are of growing concern as they pose a serious risk to aquatic biota. Recently, membrane technology was implemented as an innovative water treatment method for both oil and protein water separation[2].

Ultrafiltration membranes are increasingly applied in wastewater reclamation and recycling. They provide exceptional benefits in terms of improving effluent quality and have a much smaller environmental footprint[34]. However, they are prone to fouling, and this limits membrane performance. This fouling is caused by an accumulation of organic particles suspended in solution, solids, colloids, and microbes on the surface and pores of the membrane, which ultimately decrease the permeability and selectivity of the membrane over a period of time. Fouling can be permanent thus making it difficult to dislodge the fouling layer simply by rinsing[5]. Membrane modification is necessary in cases where the fouling is permanent[5]. The surface characteristic of membranes is critical during separation since it is the first point of contact with feed solutions. Consequently, membrane-foulant interactions can be minimized through modifying the surface properties of the membrane, such as the surface charge, and roughness, in addition to hydrophilicity. To minimize foulant interactions, several membrane modification techniques can be used to append hydrophilic functional groups onto and within hydrophobic membranes[4]. Moreover, among the known surface modification approaches, increasing the surface hydrophilicity of membranes is considered to play a critical role in minimizing membrane fouling behavior. The formation of a constant hydration layer, which disrupts particle adsorption on the membrane surfaces, is hypothesized to cause the antifouling trait of hydrophilic membranes[6,7].

To tackle this challenging issue of formation of hydration layer, extensive research has been conducted to develop suitable membranes with enhanced mechanical properties, hydrophilicity, low fouling, high water permeation, and rejection properties using a surface modification (such as coating, grafting, and others), physical blending, and other methods[8]. In the same vein, polymer blends have long been considered the most cost-effective, simple, and adaptable way of modifying and increasing the surface characteristics of polymers. The fundamental problem with polymer blending is that it necessitates the dissolution, in the same solvent, of two polymers that possess large variances in hydrophilicity. As a result, the technique is restricted by the polymer's poor miscibility[689]

We have previously developed a blend of an UF membrane that possesses high porosity and improved anti-fouling properties[10]. In this regard, hydrophilic EVOH was blended with PSF, and PEG was used as a hydrophilic additive and compatibilizer. The findings revealed that PSF/EVOH membranes have superior hydrophilicity and protein anti-fouling capabilities than virgin PSF membranes. Despite these benefits, the inherent fingerlike structures created upon blending EVOH and PSF coupled with an increase in the fingerlike structure caused by EVOH resulted in reduction in mechanical strength[10]. An increase in the fingerlike structure is known to be caused by the EVOH[10]. To enhance membrane performance, other research groups have focused on enhancing the hydrophilicity of the membrane surface by incorporating hydrophilic EVOH polymers in the membrane matrix. For instance, Miao et al.[11] synthesized polyvinylidene fluoride (PVDF)/EVOH blended membranes via immersion precipitation[11]. They discovered that the blended membrane was more hydrophilic, reducing the fouling interaction force between EVOH and BSA. Regardless of the inherent benefits, it was also revealed that an increase in the quantity of EVOH was followed by a decrease in the tensile strength of the resultant membrane. This was ascribed to the high-level of hydroxyl density of the EVOH chains. At very high concentrations, the EVOH self-

aggregates, and its distribution in the blend matrix is nonuniform. This, therefore, results in inadequate links between PVDF and EVOH and ultimately caused a decrease in the strength of the blended membrane[11]. In other studies, sulfonation treatment of polymers was used as an effective method for addressing fouling owing to the high hydrophilic nature of sulfonic acid functional groups and ease of the sulfonation reaction[12–14]. Fouling mitigation is typically achieved with sulfonated polymer chains such as sulfonated poly (ether ether ketone) (SPEEK) and sulfonated polysulfone (SPSF). However, as in the case of EVOH, these polymers cannot be added in excess because they have a negative impact on the long-term operational stability, mechanical strength, and thermal stability of membranes[15,16]. As a result, the ability of hydrophilic polymers to significantly improve membrane permeability and antifouling ability becomes limited. Fabricating at an acceptable cost a membrane that possesses high selectivity and permeability, superior stability, and antifouling capability while retaining mechanical properties remains a significant challenge and a meaningful topic for polymer materials scientists.

In addition to the above-mentioned modifications, membrane inclusion of hydrophilic nanoparticles has attracted the interest of researchers because of its ease of processing and apparent separation performance. These NPs include zero-dimensional (0D) silver nanoparticles (Ag), zinc oxide (ZnO), gold nanoparticles (Au), titanium dioxide (TiO_2); one-dimensional (1D) carbon nanotubes (CNTs), halloysite nanotubes (HNTs); two-dimensional (2D) graphene oxide (GO)[17 18]. Although limited studies have been reported in literature on the improvement of polymeric membranes employing pure HNTs, HNTs have recently gained popularity for increasing membrane characteristics and performance. HNTs have been shown to produce a more evenly distributed pattern with lower membrane leakage of NPs[19]. HNTs are a non-toxic, stable, and affordable type of 1D aluminosilicate that exists naturally as clay minerals composed of inorganic nanotubes with a Si/Al ratio of 1:1. Previous studies have demonstrated the unique properties of HNTs that can be exploited for application in water and wastewater treatment. These properties include tubular nanostructures with a rather high aspect ratio, a natural abundance that makes them readily available, good biocompatibility, strong mechanical strength, and abundant hydroxyl functional groups on the surface and within the tubes[19]. HNTs enhance water permeation as well as antifouling properties, which are brought about by the existent hydrophilic groups in the structure of HNTs.

To date, pure HNTs have been employed to produce membranes from PSF[20 21], polyacrylonitrile (PAN)[22], polyethersulfone (PES)[23 24] polystyrene (PS)[25,] and polyvinyl chloride (PVC)[26]. For instance, Mishra et al.[26] discovered that the rejection of BSA was greater than 90% for all MMMs composed of PVC/HNTs. Furthermore, a direct correlation between the amount of HNTs in the membrane dope solution and the rejection of BSA was established. Lastly, respective increases of up 212.22 L m^2 h^1 and 92.1 % in thepure water flux (PWF) and flux recovery (FRR) of PVC/HNTs were recorded. Similarly, Buruga et al.[25] have reported that the HNTs (5 wt.%) incorporated into a polystyrene matrix demonstrated outstanding thermal and mechanical capabilities as well as good PWF and FRR. The thermal stability increased from 380 ⬚C to 415 ⬚C for PS and PS/HNTs, respectively. Moreover, Mozia et al. [23] reported an improved anti-fouling

propensity of PES membranes altered with HNTs. This propensity was ascribed to an increase in the hydrophilicity and a higher negative charge on the membrane surface, which caused negatively charged BSA to be repelled. When evaluated at a pH similar to that of the BSA solution (6.85), the zeta potential of the PES/HNTs MMMs was found to be identical for all HNTs concentrations, ranging from − 36 to -38 mV. Furthermore, the contact angle for highest loading was found to be 53°.

The inclusion of HNTs into polymeric membranes was found to impact their physicochemical properties and morphologies. Hydrophilic materials provide a surface hydration layer that behaves as an energy and physical barrier, thus inhibiting fouling material from adhering. Halloysite is also negatively charged, and this contributes to membrane fouling resistance. Evidently, due to their hydrophilicity, HNTs have been consistently found to produce a membrane morphology that is characterized by finger-like features and/or macro voids covering the entire membrane cross-section[20–27]. Although finger-like macro voids in polymeric membranes generally increase water permeability, recent research indicates that controlling membrane morphology, specifically suppressing membrane cross-sectional macrovoids, is critical in improving the mechanical strength. HNTs themselves have the ability to increase the mechanical strength of membranes. The way this happens is when the composite membrane is under pressure during the filtration process, the resulting stress is primarily shifted to the HNTs in MMM instead of being distributed evenly between the membrane matrix and HNTs. Additionally, the porosity of the membranes may be altered during operation due to compaction and the creep phenomenon. The tensions caused by the pressure of the filtering process lead to membrane deterioration. When a membrane is stressed, its thickness may decrease temporarily or permanently. Compaction has an impact on the bulk porosities and material properties of polymeric porous membranes. Membrane compaction has been demonstrated to occur mostly in layers of the membrane, which contain finger-like pore structures and macrovoids. It is critical to determine methods to maximize the hydrophilicity of the membrane while maintaining its mechanical properties.

The purpose of this research is to adjust the morphology and antifouling properties of a PSF/EVOH blend membrane with relatively high mechanical strength by adding HNTs to modulate casting thermodynamics and membrane formation kinetics, that is, the synergistic effect of PSF, EVOH, and HNTs. Molecular dynamics (MD) simulations and Raman data were employed to demonstrate hydrogen bonding in the MMMs. Furthermore, the impact of HNTs on membrane parameters such as porosity, pore size, hydrophilicity, pure water flux, thermal stability, and mechanical properties, and microstructures of the membrane were examined. Finally, BSA solution and gasoline (oil)-in-water emulsion were used to investigate the separation performance and antifouling ability of PSF/EVOH/HNTs membranes.

Experimental

Materials

PSF (Mw = 35,000 g/mol, Udel P-3500) (Shanghai, China) was supplied by Solvay Advanced Polymers Co., Ltd supplied. EVOH (32% ethylene content) was purchased from Sigma Aldrich (St. Louis, MI, USA).

PEG 20 kDa (Mw = 20,000 g/mol) was supplied by Tianjin Kermel Chemical Reagent, dimethylacetamide (DMAC) by Tianjin Fuchen Chemical Reagent Co. (Tianjin, China), and BSA Mw = ~ 68 kDa by Sigma-Aldrich (St. Louis, MI, USA). Gasoline for the filter studies was obtained SINOPEC Tianjin Oil Products Corporation while sodium dodecyl sulfate (SDS) (China) was procured from Fengchuan Co. Ltd provided. Lastly, the HNT powder supplied by Runwo Materials Technology Co. Ltd, China.

Fabrication of MMM membranes

All the MMMs were synthesized using a previously described non-solvent induced phase separation (NIPS) method[4]. Before addition of polymers, previously weighed quantities of HNTs were ultrasonically disseminated in a DMAC solvent. HNTs were first ultrasonically dispersed in DMAC. Using this method, we were able to produce a uniform distribution of HNT sizes. The polymer percentage of the PSF/EVOH32/HNTs mix casting solutions was maintained at 20 wt.% of the DMAC solvent. Respective compositions of the dope solutions are shown in Table 1.

To obtain homogeneous casting solutions, quantified masses of PSF, EVOH32, PEG 20 kDa, and HNTs were suspended in DMAC at 70°C and thereafter mixed vigorously for 12 h until completely dissolved (**Scheme 1**). Casting solutions were degassed for 8 h prior to being spread evenly onto a glass sheet utilizing automatic apparatus (Elcometer 4340) and a cast membrane applier stage set at approximately 200 meters. In a coagulation water bath, the glass sheet was immersed in deionized (DI) water at 25°C. The membranes were subsequently washed with deionized water up till they reached a pH of 7. Thereafter, the membranes were soaked in DI water and put in storage until application.

The dope solutions of the composition are shown in Table 1. Increasing the amount of HNTs from 0 to 0.12 wt.% gave rise to corresponding HNTs-containing membranes, which are numbered M0–M12. Whereas M0 denotes the pristine PSF/EVOH membrane that is free of the HNTs, the corresponding membranes that contain different concentrations of HNTs were numbered M2, M3, M6, M8, and M12, respectively.

Table 1
Composition of dope solutions for the PSF/EVOH32/HNTs mixed matrix membranes.

Membranes	PSF/EVOH32 (wt.%)	PSF (g)	EVOH32 (g)	DMAC (g)	HNTs (wt.%)	PEG (20kDa) (g)
M0	95/5	10.45	0.55	39	0.00	8
M2	95/5	10.45	0.55	38.75	0.02	8
M3	95/5	10.45	0.55	38.25	0.03	8
M6	95/5	10.45	0.55	38	0.06	8
M8	95/5	10.45	0.55	37	0.08	8
M12	95/5	10.45	0.55	36	0.12	8

Characterization of fabricated PSF/EVOH and PSF/EVOH MMMs

The rheological parameters for the dope solutions were studied using a digital rotating viscometer at various temperatures and shear rate of 10 s^{-1} (NDJ-8S, Hengping Instrument Company, Shanghai, China).

The rate of membrane development was quantified using ultrasonic transmission measurements, and the link between the rate of phase inversion and membrane shape was investigated as reported in our previous work[14]. Sound propagation is the basis for ultrasonic measurements. The velocity of sound through a medium is determined by the medium's density and elastic constants (impedance). To describe and display the data, an oscilloscope was linked to the pulser–receiver. The temperature of the experimental procedure was maintained at 25 ± 0.5°C with transducers spaced about 20 mm apart. The time it takes for ultrasonic emission to occur is determined using the ultrasonic emission theory. As shown in Eq. 1, the amount of time it takes for a sound wave to travel from an emitter to a receiver is determined by the path length (S) and velocity (c). Changes in sound velocity caused by non-solvent and solvent mixing processes are thus related to membrane formation processes.

$$\Delta S = c * \Delta t$$

1

The membranes thickness was measured with a digital micrometer and the bulk porosity was determined using the gravimetric technique. The gravimetric technique requires membrane coupons to be cut to a specific size (length, width, and thickness) and dried at 50°C to eliminate water. To achieve water absorption equilibrium, the dry membrane was weighed (W_d) before being submerged in 50 ml of deionized water for 24 h. Thereafter, the wet membranes were pat dried with two filter sheets sandwiched between them.

The remaining drops of water were wiped away with fresh, lint-free cloths. The membranes were then weighed (W_w). Internal water molecules were not thoroughly removed. Metrics were calculated using the average of three replicates. Both wet and dry membrane weights were utilized to calculate total porosity. Eq. 2 was used to compute bulk porosity.

$$\epsilon(\%) = \frac{W_w - W_d}{\rho_w A \delta} \times 100\%$$

2

where ϵ is the bulk membrane porosity, ρ_w the water density (g/cm^3), A the effective section membrane of the coupon (cm^2), and δ the width of membrane cross-section (cm).

The Guerout-Elford-Ferry equation was employed to calculate mean pore radius size (nm) of the membranes centered on porosity and net water permeability results as given in Eq. 3.

$$r_m = \sqrt{\frac{(2.9 - 1.75\epsilon)8\eta L_m Q}{\epsilon. a. \Delta P}}$$

3

where η is the viscosity of water (8.9× 104 Pa s), L_m is the membrane thickness (m), ϵ is the porosity of the membrane, a is the effective area of the membrane (m^2), Q is the volume of permeate water ($m^3 s^{-1}$), and ΔP is the operation pressure (1 bar).

An attenuated total reflection Fourier transform infrared (ATR-FTIR) spectrometer was used to determine the surface functional groups present in the dried membrane samples (Nicolet™ iS50, Thermo Fisher Scientific). The FTIR spectra were measured in the wavelength range of 4000 – 450 cm^{1}.

Thermo Fisher's X-ray photoelectron spectroscopy (XPS) K-alpha was utilized to elucidate the chemical structures on prepared membrane surfaces to determine the assembly of HNTs in the PSF/EVOH/HNTs MMM. Al K (1486.6 eV) was used as the radiation source. The survey spectrum was measured from 0 to 1350 eV, including C 1s spectra.

The surface, bottom, and cross-section morphologies of the mixed membrane were examined using a field emission scanning electron microscope (FE-SEM), (S-4800, HITACHI, Japan). For imaging, the samples of the membrane were cross-sectioned in liquid nitrogen. ImageJ processing application software was used to calculate the average pore diameters on the surface. A transmission electron microscope (TEM) set at 120 kV was used for additional images. Thin slices of approximately 100 nm were cut using a Leica ultramicrotome. Membrane samples were glued with epoxy glue and then 100 nm ultrathin pieces were placed on a copper grid for imaging.

The hydrophilicity of the prepared membranes was evaluated through evaluating static and dynamic contact angles in the sessile drop mode at 25°C using the precision equipment Kruss Drop Shape Analyzer-DSA25 (Germany). A procedure involving placing a drop of DI water on dry membrane surfaces followed by capturing the contact angle with a photographic camera for 100 sec is the procedure was adopted. To limit experimental error, the measured contact angles were performed three times and a standard average value was attained.

A tensile testing machine was used to evaluate the tensile properties of the membranes (Hengyu Co., Ltd, China). Vacuum dried membrane sections of a thickness of 5×5 mm were fixed on a membrane repository, and measurements taken at a rate of about 0.5 cm/min. For each membrane, about 3 samples were measured, and an average number was calculated.

On a laboratory set-up crossflow system, the membranes performance was assessed using pure water permeance (PWP) and BSA rejection. To fit the filtration cell, membrane coupons were cut into circles with an actual area of 7.0695 cm^2. During the first hour, compression of membranes was achieved by flowing water across them at 0.15 bar. The pressure was then reduced to 1 bar in order to evaluate the water flow rate and determine PWP (Pw_1) (L m^{-2} h^{-1} bar^{-1}). The (PWP) was calculated using Eq. 4.

$$P_{w1} = \frac{V}{A\Delta t\Delta P}$$

4

where P_{w1} denotes (PWP), V (L) the quantity of water obtained, A (m^2) the membrane area analyzed, Δt (h) the working duration, and ΔP the pressure (bar).

The solute retention efficiency of the blended membrane was assessed using BSA (as the solute reference and gasoline. A mass of 1 g of gasoline and 0.5 g of SDS were added to 500 ml of deionized water and agitated for 24 hours at 500 rpm and room temperature to create a stable oil-in-water emulsion, and the collected permeate was analyzed using a Malvern Mastersizer analyzer (ZS 90, Malvern Instruments Ltd., UK). Eq. 5 was used to determine the examined rejection.

$$R(\%) = \left\{1 - \frac{C_p}{C_f}\right\} \times 100$$

5

A spectrophotometer set at 280 nm was used to measure the amounts of BSA in the feed and permeate solutions.

The feed solution concentration was maintained constant at 1 g/L for the antifouling tests. After compressing each membrane for 1 hour, the pure water permeability (P_{w1}) was calculated at 1 bar using Eq. 4. After emptying the filter cell, the BSA feed solution was added. For one hour, BSA permeance (Jp) was monitored every 10 minutes for a BSA foulant solution. The antifouling capacity of the membrane was assessed using Eq. 6 to calculate the rate of decrease in the antifouling propensity, that is, the permeance recovery rate ratio (PRR).

$$PRR(\%) = \frac{J_{w2\,VII}}{J_{w1}} \times 100$$

6

Since P_{w1} and P_{w2} refer to pure water permeability and water permeability after cleaning the membrane following BSA solution filtration, J_{w2VII} is the PWP at the final stage VII.

An oil-in-water emulsion feed was created by stirring for 8 h at 1000 rpm a mixture of 1 ml gasoline with 99 ml water with 0.1 mg SDS before leaving to stabilize for 1 hour at room temperature. The oil droplet sizes and size distributions of the emulsions were studied using a dynamic light scatterer (DLS) (ELSZ-1000ZA, Otsuka Electronics, Japan) (BX50, Olympus, Japan). The permeate content of oil was determined using a Total Organic Carbon Analyzer (TOC-VCSH, Shimadzu, Japan).

The optimized structure of HNT with PSF, EVOH, and PEG polymer chains were chosen as MD probes. In this system, the x and y dimensions were periodic constraints, while the z dimension was flexible. Subsequently, MD simulations were performed following a procedure described in our previous work[10].

Results And Discussion

Physico-chemical properties of HNTS

The HNT nanoparticles with a length of 0.2–2 μm, an outer diameter of 40–70 nm were sonicated in DMAC before being transferred to a McCartney flask. A murky dispersion with an HNTs concentration of around 0.1 g L^1 was made (Fig. 1). Owing to the weak tube-tube interactions, the HNTs dispersion is stable and can be stored for at least one week. As suggested by Zhou et al.[27]., HNTs can be dispersed well in solvents with solubility parameters ranging from 22.5-36.7MP (relevant information provided in **Table S1**[27]).

DLS, SEM and Transmission electron microscopy energy-dispersive X-ray (TEM-EDX) spectroscopic techniques were employed to examine the structure of the nanotubes (see Fig. 1). According to the DLS results depicted in Fig. 1**(a-b)**, the HNTs with an average length of 340.7 ± 3.09 nm exhibited an excellent dispersity in ID water. The SEM microscopy revealed that the halloysite and its calcining products have an interior portion open-ended needle shape. The samples under consideration concur with previously reported sizes and length/diameter ratios[19]. Further, TEM analysis was also utilized in conjunction with EDX spectroscopy to investigate the shape and elemental content of the core-shell nanostructures, and the results are depicted in Fig. 1 **(c)**. The inner region of HNTs is hollow and open, according to TEM images of the halloysite. Elemental analysis using core-shell nanostructures at the designated site confirmed the elemental composition of the basic elements stated in the literature as well as the fact that clay and mineral are composed of O, Al, Si[23,26].

Dispersion of HNTs in PSF/EVOH matrix and H-bonding interaction analysis

The stability and dispersion of the HNTs in the dope solutions were assessed immediately following preparation of the fresh samples, and after storing the samples for 4 weeks at 25°C and thereafter reheating them to 70°C. As shown in Fig. 2, no changes in the dispersion and stability of the samples were observed, and the solutions of the respective samples were both stable and homogenously blended even after storing for 4 weeks and reheating. This suggests that the dispersion and interfacial bonding of

the HNTs with the polymer solution are sufficient. Furthermore, a visual inspection of the PSF/EVOH membrane matrix possessing varying HNT loadings revealed that the additional HNTs were evenly distributed in the solutions because the intensity of the color increased with the loading concentration[28].

The type and concentration of additives are two of the most important parameters that influence the thermodynamic behaviour of the casting solution. PSF/EVOH casting solutions with varying additive loadings of HNTs were prepared, and their viscosities were measured. This is because the viscosity of the casting solution affects the kinetics of phase separation during NIPS and by extension the final membrane structure. The viscosity is, therefore, an important parameter for determining the phase separation kinetics of the casting solutions. A second parameter, temperature, also influences the casting solution behaviour and, as a result, the kinetics of membrane formation and the morphology of the membrane[4]. Figure 3 depicts the link between temperature and casting solution viscosity at various concentrations of HNTs. It is evident from Fig. 3 that an increase in temperature results in a decrease in the viscosity of the M0-M12 samples. For example, when the temperature was increased from 44 to 55 ⬚C, the viscosity of the M0 sample decreased from 1520 to 1290 mPa s. The decrease in viscosity is attributed to a rise in molecular kinetic energy intensity at high temperatures, resulting in increased polymer chain mobility[28].

Additionally, as shown in Fig. 3, the viscosity of the casting solution increased rapidly when the loading of the HNTs was increased from 0 wt.% (M0) to 0.12 wt. % (M12). For example, at 55°C the viscosities of the various samples increased as follows: 1290 mPa s for M0, 1360 mPa s for M2, 1780 mPa s for M6, and 2358 mPa s for M12. The type of the donor and acceptor determines the strength of a single hydrogen bond; the strength of each hydrogen bond tends to increase when numerous hydrogen bonds form at the same time. In this study, the increase in the viscosity is ascribed to adsorption and development of numerous hydrogen bonds afforded by the high specific surface area restricting the mobility of the polymer chains[29]. This is especially true for HNTs nanoparticles which possess additional various atomic groups that participate in the formation of bonds between HNTs and PSF, EVOH, and PEG polymers. This was confirmed by MD simulations. On the edge surfaces and defects of HNTs surfaces, there are Si−O, Al−OH, and hydroxyl groups (−OH). In particular, the prospect of a unique role played by the terminal hydroxyl groups (−OH) of the EVOH polymer chains and the sulfone (-SO$_2$) groups of the PSF polymeric chains to form hydrogen bonds with the HNTs should be noted.

In other words, the quantity of hydrogen bonds formed amongst the dope solution components evidently increases when the amount of HNTs increases, with the added benefit of limiting HNTs aggregation and promoting uniform dispersion. During the phase separation process, the casting solutions increase the viscosity usually induces reduction in the diffusion rate between solvent and non-solvent, which causes delayed demixing. This leads to the suppression of macrovoids in the membrane underlayer, the creation of a denser structure, and improved mechanical strength properties. In the following sections, the effect of viscosity on the membrane structure is discussed in more detail.

To investigate hydrogen bonding interactions in solutions, vibrational spectroscopy techniques (IR and Raman) are used[30,31]. Figure 4 **depicts** Raman spectra generated from M0 as well as M12 dope solutions. Appearing at 1153.90 cm^{-1} is the peak attributed to the C-S stretch of PSF in M0. However, when HNTs were added to the casting solutions, the C-S stretching vibration peak of PSF in M12 shifted from 1153.90 cm^{-1} to 1150.20 cm^{-1}. This red shift was attributed to the Hydrogen bonding that exists with HNTs and PSF in M12, which resulted in electron cloud distortion of -SO$_3$ atoms. Fan et al.[31] made a similar observation, they found that the stretching vibration peak in the PES/PEG2000-m-trihydroxy benzene composition red-shifted to a longer wavelength from 1159 to 1156 cm^{-1} owing to H-bonding interaction.

In many miscible polymer composites, H-bonding commonly forms inside the same polymer or between molecules that are in close proximity to each other. H-bond is the attraction between donor and acceptor atoms at a distance of 2.5 to 3.5 Å. MD simulations was used to evaluate the putative H-bond interaction in the PSF/EVOH/PEG/HNTs system. The radial distribution function depicts likelihood of encountering another atom at a certain distance (r), which is related to the H-bond interaction[32,33]. Figure 5**(a)** depicts the structure of the system while the radial distribution function (RDF) calculation is described in Fig. 5**(b)**. The RDF of the bonds between PSF and HNTs, HNTs and PEG, and EVOH and HNTs shows that the strongest intramolecular hydrogen bonds (H-bonds) are formed between HNTs and PSF. This is evidenced by the first peak appearing at about 2.68 Å, which relates to the PSF polymeric chains forming direct H-bonds with moieties of the HNTs. In addition, EVOH and HNTs, PEG, and HNTs also show strong hydrogen bonding interactions, and this is evidenced by the first peaks appearing at about 2.89 Å and 3.19 Å respectively. Finally, the H-bond interactions make HNTs more stable and evenly dispersed in polymer solutions thus efficiently preventing nanoparticle aggregation. In general, the MD simulations agree with the above-mentioned experimental results.

Physico-chemical properties of MMMs

The FTIR spectra of halloysite nanoparticles, pristine PSF/EVOH membrane (M0), and PSF/EVOH/HNTs MMMs are shown in **Fig.S1.** Evidently, the peaks at 3693 cm^{-1} and 3616

cm^{-1} are associated with the OH bond stretching vibration of the inner surface of the Al-OH groups and the inner Al-OH groups between the interface of the Si-O tetrahedron and the Al-O octahedrons on raw HNTs (**Fig. S1(b-c)**). The in-plane Si-O stretching vibration is evidenced by the peak appearing at 1030 cm^{-1}. The peak at 910 cm^{-1} represents the OH bending vibration of the interior Al-OH groups. As shown in **Fig. S1(a)**, the Al-O-Si and Si-O-Si bonds are ascribed to the peaks at 538 and 468 cm^{-1}, respectively [34].

Additionally, the peaks at 2900 and 3300 cm^{-1} that appear in the spectra of the pristine PSF/EVOH membrane are attributed to the symmetric and asymmetric vibrations of the CH$_2$ and OH groups, respectively, and they reveal the unique structure of PSF/EVOH32 (**Fig. S1(c-d)**)[10,35]. The spectrum of the PSF/EVOH/HNTs MMMs shows the presence of major absorbance peaks ascribed to the HNTs, thus

providing evidence for the presence of HNT inside the membrane pores. A new peak was observed at 3694 cm^{-1}, and this is assigned to the shift of original peaks Al-OH (3500 cm^{-1}); for MMMs, peak shifts generally appear between 3500 cm^{-1} and 3694 cm^{-1}. A possible reason for the peak shift may be because of the interaction between the Al layers of HNTs and the polymer blend. Following mixing, the variations in frequency associated with the O-H bending and stretching decreased in MMMs. As shown in **Fig. S1(c)**, in the presence of large O-Si-O groups, the asymmetric flexible vibration of O-Si bonds on the exterior of the HNTs generated a strong peak in the HNTs (at 1030 cm^{-1}), which shifted slightly to 1040 cm^{-1} due to the interaction between Si-O and the base polymer. It is important to note that there is an overlap between the absorption peaks of the HNTs and PSF/EVOH polymer, which is evident in **Fig. S1**. It is feasible to deduce from these FT-IR measurements (**Fig. S1**) that because of an existing overlap of HNTs and PSF/EVOH polymer absorption peaks further distinctive absorption peaks of the HNTs in the membrane spectrum could not be easily distinguished. It is therefore imperative to use SEM EDX mapping and XPS analysis to confirm successful integration and HNTs dispersion in the polymer matrix membrane [26].

The chemical compositional changes of the membrane surfaces (M0 and M12) were investigated by XPS analysis, and the results are shown in Fig. 6 and **Table S2**. Therein, S2p, C1s, and O1s were represented by three significant peaks produced from M0 at 168.14 eV, 285.07 eV, and 532.27 eV, respectively. It is apparent from Fig. 6 **(b)** that PSF/EVOH/HNTs MMMs (M3) exhibited a similar effect. In addition, a new Si peak obtained from M3 emerges at 102.31 eV. The atomic concentration of O1s produced from M3, on the other hand, was 22.99%, which was greater than that of M0 (20.43%) (**Table S2**). The effective addition of HNTs into PSF/EVOH matrix was ascribed to the increased atomic concentration of the O1s. Further, as shown in Fig. 6 **(c)**, three typical emission peaks of M0, which appear at 286.3 eV,284.8, and 285.1, were assigned to C-O, C-C, and C-S bonds, respectively[39]. A new emission peak was seen at 284.1 eV for M6, and this was assigned to C-Si groups of the HNTs. In a nutshell, spectral analysis revealed that the PSF/EVOH/HNTs MMMs were successfully fabricated and evidence of an existence of a strong H-bond interaction between HNTs and polymer matrix was observed.

Membrane formation and characterization

HNTs have considerable impact on the properties of casting solutions. Additional research was carried out to corroborate the impact of HNTs on the properties of the membrane. As shown in Fig. 7, FE-SEM analyses were used to investigate the surfaces and cross-sectional morphologies of flat membranes. Figure 7 demonstrates that the surfaces of all membranes are reasonably smooth, with no accumulation of HNT bulk or clumps were observed. This implies that the HNTs nanoparticles were evenly distributed throughout the polymer matrix. Furthermore, no surface cracks were observed, indicating MMMs did not become brittle and were rather stable after the addition of the HNTs. In fact, many nanoparticles used for synthesising MMMs (e.g., TiO$_2$[37] and HNTs[38]) are visible on the membrane surface of membranes synthesised via the phase inversion approach. Emadzadeh et al.[38] have reported that considerable aggregation on the surface impairs the structural stability membrane.

In contrast, Fig. 7 shows a variation in the cross-sectional SEM images of the fabricated membranes. In addition, all the fabricated membranes were found to possess an asymmetric structure when the concentration of the HNTs was increased. The MMMs with a low loading of HNTs (0.02–0.03 wt.%) formed an asymmetric morphology with a skin layer, sponge-like sublayer, and macrovoids substrate (Fig. 7a-c). Increasing the HNTs loading (> 0.06 wt.%) gradually altered the membrane microstructure. However, the finger-like structures/macrovoids were suppressed and eventually eliminated when with increasing HNTs loading (see SEM images of M6-M12 in Fig. 7 (d-f)). In general, at low concentrations of the HNTs in the casting solution, macrovoids form in MMMs and become run-through. However, at a higher filler concentration, they are suppressed.

Clearly, this structural change corresponds to the phase transition of the corresponding thermodynamics of the casting solution thus indicating a synergistic H-bonding effect of HNTs with polymers (PSF, EVOH, and PSF). Usually, these H-bonds increases the viscosity of dope solutions and subsequently slows the rate of solvent and non-solvent double-diffusion in a coagulation bath. Specifically, the solvent (DMAC) and nonsolvent (water) diffusional rate decrease during the solidification process preventing immediate demixing. In other words, the kinetics of the MMMs formation was affected by the delay in the demixing. This delay produces a sponge-like structure with uniform distribution of the HNTs in the polymer matrix, which is ultimately ascribed to the formation of the H-bond between PSF/EVOH base polymer and HNTs.

In addition, higher magnification SEM images were used for a further comparison of the microstructural variations of M0 and M6 (see Fig. 7(g) and Fig. 7(h)). It is evident in Fig. 7(g) that M0 displayed a typical asymmetric structure with a thick skin layer, sponge-like sublayer, and macrovoids substrate. Interestingly, M6 exhibited an asymmetric structure with a thin skin layer and a fully sponge-like sublayer (Fig. 7(h)). In particular, larger cellular cavities in the sublayer were evenly distributed in the polymer matrix; it is envisaged that this will provide a low water transfer resistance in the membrane filtration. In summary, adding HNTs to the dope solution changed the thermodynamics and kinetics of the membrane formation process, resulting in a range of membrane morphologies, properties, and performance described in more detail in the next sections.

Cross-section Surface

To establish the presence and distribution of HNTs in the PSF/EVOH membrane matrix, TEM and SEM-EDX analyses were performed on the membrane with 0.06 wt.% loading (M6) (see Fig. 8 (a)). The TEM images showed that HNTS were relatively evenly distributed as dark gray spots in the PSF/EVOH matrix, and they exist as separate nanotubes with no entanglement or agglomeration segments. In particular, the cylindrical structure of the HNTS-PSF/EVOH matrix was also observed. This indicates that the HNTs dispersion in the membrane is homogeneous. This dispersion may result from the higher density functional groups (O, OH, and Al) availability on the HNTs (see Fig. 8 (b)), which benefits an effective interaction with a polymer matrix that was previously confirmed by Raman and FTIR spectroscopies. The even distribution of HNTs in the PSF/EVOH membrane allows for improvements in structural properties, notably mechanical strength, which is elaborated on in the latter sections of this work.

In fact, the mutual diffusion rate between the solvent and nonsolvent is high at low concentrations of HNTs, and this results in macro void/finger-like structures that are caused by instantaneous demixing. The mutual diffusion rate becomes low enough to limit the growth of finger-like macro-voids via delayed demixing. Finally, the macrovoids disappear when the composition of the HNTs reach 0.06 wt.% – 0.12 wt.%. This is because the high viscosity of the casting solution slows non-solvent diffusion thus lowering the rate of phase inversion. Therefore, the formation mechanism of PSF/EVOH/HNTs MMMs is proposed in Scheme 3.

We have previously reported that the shifting of the ultrasonic signals in the time domain can be monitored to assess or quantify the effect of HNTs on membrane formation[36]. Typical ultrasonic spectra of transmission signals (Peak A) amplitude in volts (V) versus arrival time in seconds (s) during membrane development from virgin polymer solutions and blend HNTs solutions are shown in Fig. 9. Essentially, a transducer generates ultrasonic wave pulses that travel through coagulation baths, casting solutions, and glass. The amplitude of the pulses versus arrival time spectra are then computed.

Figure 9(a) shows that the ultrasonic signals moved at a faster rate at the start of membrane formation, resulting in increased velocity. However, when the skin layer was formed, mutual diffusion was inhibited until equilibrium was reached, and it gradually decreased after 30 s. This is because the rate of DMAC solvent diffusion into the bath decreased until equilibrium was reached, however, when the skin layer was formed mutual diffusion was inhibited until equilibrium was reached and a dense skin layer formed.

The ultrasonic velocity through the media resulting from changes in the thermodynamic behavior as well as changes in the density of the mixture affected the attenuation and shift in arrival time during the formation of the dense skin. Figure 9(b) shows the time-domain decreased upon addition and increase in the concentration of the HNTs. While the ultrasonic signals shifted rapidly for the pristine M0, a low ultrasonic velocity was recorded for the membrane matrix with low HNTs (M0, 0.03 wt.%). After immersion for 10 s, the arrival time did not change as rapidly as with the membrane matrix with a high HNTs (0.12 wt.%). The casting solution's viscosity increased when the HNTs concentration was increased. This change in the viscosity is owed to the development of strong H-bonds between PSF, EVOH, PEG, and the HNTs (Fig. 9), which prevent the DMAC from disseminating into the coagulation water bath. The increased ultrasonic velocity is caused by the rapid diffusion rate. As a result, as seen in Fig. 9(b), ultrasonic signals in the time domain shift became lower when the HNTs was increased with increasing HNTs[14][36]. From the results, it can be concluded that adding HNTs to the PSF/EVOH dope solutions has a greater effect on the rheological and phase separation behavior of the dope solution owing to the inherent strong interactions that exist between the HNT_S and PSF/EVOH. In a nutshell, the acoustic observations are in line with SEM analysis and the schemed membrane formation mechanism.

Properties of blend membranes

Table 2 shows the results of several characterization tests (top surface porosity, average porosity, and average pore size) performed on all fabricated membranes in this work. Since the experiments were

reproduced three times, the standard deviation for all results is comparably given in Table 2. According to Table 2, the mean pore radius of the MMMs increased slightly from 30.67 ± 1.28 (M0) to 37.57–38.92 nm (M8-M12) with the inclusion of the nanomaterial. Similarly, increasing the HNTs loading in membranes resulted in an increase in the mean pore size of MMMs from 12.8 nm to 23.6 nm. Further, the porosity values ranged from 82.7 ± 2.1% (M0) to 87.5 ± 3.4% (M12).

As mentioned, each membrane was found to possess thick top surface (Fig. 7). Furthermore, the thickness of the blended membranes rapidly reduced from 124 µm (M0) to 115 µm, then increased to 122 µm (M12) when the HNTs composition of the membrane was increased (Table 2). Commonly, a low-viscosity casting solution leads to instantaneous demixing or a rapid solidification of the film, resulting in a membrane with a relatively high thickness. A high-viscosity solution easily results in delayed mixing, which provides enough time for polymer chains to rearrange thus bringing about a reduced thickness. A high HNT concentration in the polymer solution would most certainly lead to MMMs with an increased thickness.

Table 2
The properties of membranes

No.	Bulk porosity (%)	Mean pore radius (nm)	Mean surface pore size (nm)	Thickness (µm)	Contact angle (°)
M0	82.7 ± 2.1	30.67 ± 1.28	12.8 ± 2.4	124 ± 3.18	71.76 ± 2.4
M2	84.6 ± 1.6	32.39 ± 1.67	14.9 ± 2.6	115 ± 3.01	66.41 ± 2.1
M3	85.4 ± 3.0	33.44 ± 1.20	16.2 ± 4.3	117 ± 2.26	58.54 ± 3.2
M6	86.9 ± 4.1	35.87 ± 2.38	18.6 ± 2.6	119 ± 1.94	55.11 ± 1.8
M8	87.7 ± 2.6	38.92 ± 2.34	23.6 ± 3.2	121 ± 2.42	49.54 ± 2.2
M12	88.5 ± 3.4	37.57 ± 1.26	21.5 ± 1.2	122 ± 2.14	47.42 ± 1.9

Furthermore, as shown in Fig. 10, the contact angles of the prepared membranes were determined to assess the hydrophilicity and wettability of the membranes. According to Fig. 10, the pristine membrane (M0) has maximum contact angle because of its restricted hydrophilicity emanating from the hydrophilic nature of the PSF. The contact angle of the MMMs decreased significantly when the nanoparticle concentration was increased; this reveals that the addition of nanoparticles can improve the hydrophilicity of the membranes. The presence of HNTs and EVOH on the membrane surface generally leads to the presence of polar groups that participate in bond formation through van der Waals forces and hydrogen bonds. These polar groups can interact with water molecules. As a result, the water

molecules are better adsorbed and thus penetrate more easily through the membrane. When compared with the other membranes studied in this work, the membrane with the highest HNTs concentration (0.12 wt.%) exhibits the highest hydrophilicity[26,37].

Likewise, Fig. 10 (b) represents the underwater oil contact angles of the PSF membrane and the PSF/EVOH/HNTs-MMM. Underwater oil contact angles increased from 137.8° for M0 to 168.5° for M12 when the concentration of the HNTs was increased. This implies that oil droplets can be prevented from spreading by HNT-induced hydration microdomains on the surface of MMMs. The ability of MMMs to resist oil droplets improves because of the inclusion of HNTs[38]. These results also indicate that an increase in hydrophilicity of this magnitude benefit a reduction of MMMs fouling, particularly organic fouling. In water purification applications, the hydrophilic and more wettable surface layer often delivers superior water permeability and fouling resistance.

The surface charge attribute of the membrane also poses substantial impact on fouling throughout the membrane filtration process[42]. The interaction between the foulants as well as membrane can affect the deposition as well as adsorption of pollutants on the surface of membranes via electrokinetic properties. To balance the charge between the immobilized and diffused layers in the shear plane, the surface charge of a membrane or particulate matter in solution results in the development of an electric double layer consisting of a fixed layer and a diffuse layer. The zeta potential (ZP) is the electric potential produced by movement of ion at the shear plane. Hence, ZP can be calculated by measuring the streaming potential[39]. The ZP of the pristine PSF/EVOH membrane and the PSF/EVOH mixed matrix at various pH levels (3 to 10) are shown in Fig. 11. The pH was controlled using a combination of 1 M HCl and NaOH solutions. Compared to the pristine PSF/EVOH membrane (M0), the MMMs have a lower potential at each pH value. Further, surface negative charge of the membrane increased when the concentration of HNTs in the MMMs rose. M12 displayed the highest overall negative charge.[40] Generally, the overall negative surface charge of these membranes makes them promising candidates for addressing fouling and biofouling because fouling agents are frequently found to be negatively charged[41].

Mechanical and thermal properties are critical in industrial membrane applications for long-term stability. The tensile strength, as well as elongation ratio at break results, are displayed in Fig. 12. When the HNTs concentration was increased from 0.03 wt.% to 1.2 wt.%, the tensile strength of the membranes improved from 2.9 to 6.2 MPa. This dramatic increase in the tensile strength indicates that the inclusion of HNTs strengthens greatly the mechanical intensity of the MMMs. The reason for this observation has also been addressed previously. That is to say, the compatibility of the HNTs with the PSF/EVOH matrix is also linked to the exceptional mechanical properties, which are in turn associated with the characteristic high aspect ratio and huge surface area. This suggests that the HNTs nanotubes are decorated with many Si-OH and Al−OH functional groups, which participate in H-bonding in polymeric chains and increase their rigidity and elasticity [42]. As shown in Fig. 12, the results of this study revealed that HNT nanoparticles interact with the main polymers PSF and EVOH. Specifically, HNTs could act as a crosslinking point in

MMMs, allowing polymer chains to be linked and strengthened. As a result, additional energy is needed to break the strong interaction between HNTs and PSF/EVOH polymers. Furthermore, the mechanical strength of the MMM has also been improved because no filler aggregation in the polymeric matrix and visible defects on membrane surfaces were observed. At low concentrations, the HNT nanoparticles could be uniformly dispersed in the polymer solution and therefore had good adhesion to the polymer matrix.

Moreover, according to the thermogravimetric analysis (TGA) curves of the neat blend membrane and MMMs (see **Fig.S4**), a significant weight loss at about 400 ⬚C was observed. When compared with MMMs (e.g., M6), the pristine membrane the M0 (PSF/EVOH) membrane appears to degrade at a temperature of about 464.6 ⬚C. However, when 0.06 wt.% HNTs were added to the matrix, M6 displayed a higher decomposition temperature of 477.9 ⬚C. This suggests that HNTs significantly increase the thermal stability of MMMs. It can be reasoned that the interaction of HNT nanoparticles with PSF/EVOH led to an increase in the polymer chains' strength, thus making it more difficult to break down the MMMs. These TGA results, which reflect the mechanical strength of the MMMs, are comparable with results of a previously published research study[14].

Blend membrane separation performance

An inherent asymmetric membrane structure imposed by the HNTs affected the PWP of the resultant MMMs in a significant manner. Owing to the dense top surface and low porosity, the water permeance of M0 ($246 \ L \ m^{-2} \ h^{-1} \ bar^{-1}$) was the lowest, as shown in Fig. 13 **(a)**. An improvement in the PWP of the MMMs was in the following order: M12 ($419 \ L \ m^{-2} h^{-1} \ bar^{-1}$) > M8 ($398 \ L \ m^{-2} h^{-1} \ bar^{-1}$) > M6 ($383 \ L \ m^{-2} h^{-1} \ bar^{-1}$). The highest increase in the PWP (~1.7-fold) was achieved at the highest HNTs loading. This behavior correlates with large mean pore diameters (18.6 nm, 23. nm, and 21.5 nm) achieved for M6, M8, and M12, respectively. In addition, enhanced porosity, pore connectivity, and surface hydrophilicity **(Table 3)** were observed for these MMMs when compared with the pristine membrane.

As a whole, increased PWP is justified for three reasons: First, the adsorption and hydrophilicity effects of HNTs influenced non-solvent and solvent exchange during phase inversion, causing HNTs to align uniformly within and on the surface of the MMM and thereby promoting water transport. Second, increased hydrophilicity draws water into the membrane pores, allowing for easy flow of water through the membrane and thereby increasing permeability. Third, the HNTs have a cylindrical hollow submicron nanotube shape that permits water to stream through, as proposed in **Scheme 4**. Fundamentally, addition of HNTs onto the polymer matrix on one hand improved water molecule solubilization and diffusion into the membrane matrix, thereby aiding water penetration through the membranes. On the other hand, the formation of interfacial gaps of embedded HNTs and the presence of HNT lumens created more regulated pathways for water molecule permeability.

Further, the MMMs were employed to treat BSA solution (1.0 g/L) and oil-in-water emulsion (average particle size of 580.0 nm) at 1 bar operating pressure, as depicted in Fig. 13 **(b)**. It can be seen from Fig. 13 **(b)** that solute permeance of membranes for the treatment of BSA solution gradually improved

from 145 L $m^{-2}h^{-1}$ bar^{-1} (M0) to 235 L $m^{-2}h^{-1}$ bar^{-1} (M12) when the HNTs was increased from 0 to 0.12. wt%. For the membranes produced, the order of magnitude of solution permeability (SP) was determined as follows: 235 L $m^{-2}h^{-1}$ bar^{-1} for M12 > 221 L $m^{-2}h^{-1}$ bar^{-1} for M8 > 192 L $m^{-2}h^{-1}$ bar^{-1} for M6 > 192 L $m^{-2}h^{-1}$ bar^{-1} for M3 > 179 L $m^{-2}h^{-1}$ bar^{-1} for M2 > 145 L $m^{-2}h^{-1}$ bar^{-1} for M0. Similarly, the solute permeance of M12 for oil-in-water emulsion (188 L $m^{-2}h^{-1}$ bar^{-1}) was found to be higher than that of M0 (119 L $m^{-2}h^{-1}$ bar^{-1}). Clearly, all the membranes exhibited lower solute permeance than their respective PWP, which was a direct result of reversible solute adherence. Regardless the solute permeance of MMMs for both BSA and oil-in-water feeds increased with increasing concentrations of HNTs. Evidently, the permeance of MMMs obtained from BSA filtration was higher than that obtained from the treatment of the oil-in-water emulsion. The reduced oil-water solution permeance was caused by the deposition of an oil layer on the membrane surface or by oil droplets clogging the membrane pores, as illustrated in **Fig. S4(c)**, where the oil droplet size distributions of synthetic oil-water emulsions ranged from smaller to larger sizes. Further, the roughness of the MMMs (as seen in **Fig. S3**) increased when the loading of the HNTs was increased. This may also contribute to smaller oil sizes becoming lodged in crevices and settling beneath the water ultimately forming a barrier on the surface of the membrane thus preventing water from penetrating the membrane. Overall, the hydrophilic and porous properties of PSF/EVOH membranes containing HNTs allow selective water permeation from oil-water mixtures.

Additionally, as shown in Fig. 14 **(b)**, all the membranes had a BSA and oil-in-water emulsion rejection of more than 90% thus demonstrating that the modified membranes are capable of successfully retaining protein and oil molecules. However, when the amount of HNTs in the membrane increased, notably around 0.06 to 0.08 wt.%, the porosity and pore size of the membrane increased dramatically thus leading to a slight decrease in BSA and oil rejection. In contrast, the rejection increased again when the HNT content was increased to 0.12 wt.% owing to a denser skin layer. As previously described the high concentration of HNTs increased the viscosity of the solution and this affected the phase-inversion process. Ultimately, hindering the exchange of solvent and non-solvent during the phase separation process, causing the membranes to precipitate more slowly. Therefore, a porous membrane that was considerably smaller with a thicker dense layer was developed. Nonetheless, the rejection performance of the PSF/EVOH/HNTs membranes remained relatively high (over 90%.) for BSA and (85%) for oil. This was most likely because of the following two factors. First, the MMMs became more hydrophilic due to the presence of hydrophilic groups of the HNTs and EVOH on the surfaces of the MMMs. Owing to the interactions between the groups and water molecules, water molecules were easily attached to the membrane surfaces thus generating a thin hydration layer between the foulants and the membrane surfaces. This hydration layer has the potential to promote membrane permeability while also preventing the BSA from being in contact with the membrane surfaces. Secondly, at neutral pH, BSA is negatively charged, and PSF/EVOH/HNTs membranes are likewise negatively charged (Fig. 13), thereby hampering adhesion to the surface of the MMM through electrostatic repulsion. In general, the membrane retains solute with a larger size or molecular volume compared to smaller solutes with a smaller size or volume. The increase in permeance was caused by the previously described structure and inherent properties of

the MMMs, which are brought about by an increase in the concentration of the HNTs. The MMMs exhibited higher water permeance as well as BSA and oil permeance than the pristine PSF/EVOH membrane.

Moreover, the antifouling properties of the prepared membranes were tested using facile sequential PWP-fouling with 1 g/L BSA and 1000 ppm gasoline cleaning technique. Since fouling has a substantial impact on membrane performance and long-term stability, understanding membrane fouling is crucial for membrane filtration systems that explore interactions between oil droplets, BSA, and MMM surfaces [10,37,41,43].

A comparative analysis of time-dependent water permeability and BSA permeability of MMMs during fouling measurements is illustrated in Fig. 14(a). Three levels of pure water permeation (I, III, and V) and two levels of fouling (II and IV) with BSA solutions were evaluated for antifouling performance. The membranes were cleaned with deionized water after each fouling stage and the PWP was measured. Initially, the PWP remained essentially stable. Thereafter membranes became noticeably contaminated when the feed solution was adjusted to 1 g /L BSA solution. Despite decreasing from its initial value, the membrane permeability recovered after washing with deionised water. The inherent asymmetric structure of the membranes imposed by the HNTs affected the overall PWP in a significant way. According to Fig. 14 (a), the initial PWP of M0 decreased from 246 L $m^{-2}h^{-1}$ bar $^{-1}$ to 211.13 L $m^{-2}h^{-1}$ bar $^{-1}$ and finally to 201 L $m^{-2}h^{-1}$ bar $^{-1}$ after stages III and IV, respectively. The decrease in the permeance after cleaning is most likely caused by irreversible adsorption of foulants. The MMMs demonstrated a more steady restoration following the BSA filtration stage. For instance, M12 with the highest HNT loading only decreased from 419 L $m^{-2}h^{-1}$ bar $^{-1}$ to 410 L $m^{-2}h^{-1}$ bar $^{-1}$ and finally to 407 L $m^{-2}h^{-1}$ bar $^{-1}$ at the final stage. Eq. 6 was also used to compute permeance recovery ratios (PRR), which provided a more quantifiable method of measuring membrane antifouling properties. The PRR is an important parameter for assessing membrane antifouling properties; a higher PRR percentage indicates a superior antifouling performance. Figure 14 (b) shows the PRR of pristine PSF/EVOH and HNTs modified PSF/EVOH membranes when BSA and oil were used as model foulants. The PRR percentage for all the modified MMMs following 120 min of BSA permeation (97.8%) was higher than that of M0 (83.5%) after three cycles of physical cleaning with deionized water.

The PRR of blend membranes for both BSA and oil was determined to acquire better interpretation of the antifouling ability of the membranes. The PRR of M2, M3, M6 M8, and M12 after 120 min of operating with the BSA solution was 89.1%, 93.9%, 95.5%, 96.6%, and 97.8%, respectively. This could be attributed to the fact that basic water-powered cleaning effectively removes BSA molecules resulting in a high PRR. The apparent reduction in permeation of the pristine PSF/EVOH after three cycles of usage indicates poor antifouling performance. According to Fig. 14 (b), the PRR for oil filtration data was reduced throughout these three cycles for all the membranes owing to the properties of the oil emulsions (Fig. S4). The MMMs still maintained a relatively high PRR. Even after the second oil fouling and deionized water cleaning stage, the PRR of MMMs (M2 to M12) (over 85%) was greater than that of M0 (76.5%). The PRR of M2, M3, M6, M8, and M12 was 85.7%, 90.5%, 93.8%, 94.4% and 95.5%, respectively. The reason for the

sluggish recovery in PRR is that smaller-sized oil droplets (**Fig. S4(b)**) remain on the surface of the layer or block the pores from the inside after a simple pressure-driven cleaning process thus making it difficult to clean and dislodge smaller droplet sizes of oil from the membrane pores with deionized water.

As mentioned before, successful introduction of hydrophilic functional groups to the polymer matrix, which was confirmed by FTIR (**Fig S1**) and XPS (Fig. 6) and further corroborated by the high hydrophilicity of the HNT-loaded MMM, results in higher BSA and oil adsorption resistance and is therefore responsible for the outstanding antifouling performance of the membranes. The water contact angle measurements support these findings. as the concentration of HNTs increased hydrophilicity, the contact angle of MMMs decreased from 0 to 0.12 wt.%, from 71.76 ± 2.4 to 47.42 ± 1.9, as shown in Table 2. Owing to the intrinsic hydrophilic properties of the MMM, a water layer forms on the membrane surface thus avoiding direct contact between the model foulants (BSA and oil) and the membrane surface. Furthermore, the charged nature of the solute and membrane surface, colloidal behavior, and Donnan exclusion are all the factors that also influence rejection. According to the Donnan exclusion principle, the negatively charged nature of HNTs MMMs (Fig. 11) can affect the fouling resistance of modified PSF/EVOH HNTs MMMs, in addition to the effects of high hydrophilicity and hydration layer generation. These findings are in line with other previously reported studies [19]. The antifouling properties of the membrane against the BSA protein and oil molecules are improved by HNTs in the PSF/EVOH matrix.

Finally, a graphic illustration of the separation mechanism for PSF/EVOH HNTs MMMs is depicted in **Scheme. 5**. Herein, Table 4 summarises the findings of various researchers on membrane performance, which show that the PSF/EVOH/HNTs membrane have superior flux and antifouling properties.

Table 4
A review of the literature on the effect of HNT nanoparticles on morphology, properties, and performance of MMM.

Material	HNT (wt.%)	Tensile strength (MPa)	BSA rejection (%)	FRR (%)		Water permeance (LMH bar^{-1})	Ref
				unmodified	modified		
PSF$^\triangle$	0.2-5	-	99	77	98	110	21
PES$^\triangle$	0.01−0.2	1.88	98.5	58.7	92	346	24
PVC$^\triangle$	1−3	34.96	93	77.2	92	212	26
CA$^\triangle$	1−3	~ 5.5	-	66.7	89.7	92.9	50
SHBPES$^\triangle$	3−8	-	98.8	32.8	70.9	351.6	32
PSF/EVOH*	0.02−0.12	6.54	>95	81.6	97	419	This study

$^\triangle$Finger-like structures; *Sponge structure; LMH = L m^{-2} h^{-1}

Conclusion

In this study, macrovoid-free asymmetric MMMs were fabricated via NIPS from PSF using EVOH, PEG, and HNTs as additives to improve permeability and antifouling. A series of theoretical and experimental tests were conducted to assess the influence of the synergy between HNTs and the base polymers, PSF and EVOH, on the thermodynamics of the casting solution and the kinetics of membrane formation. The effect of the concentration of the HNTs on the properties and performance of the fabricated membranes was subsequently investigated. Hydrogen bonding between terminal hydroxyl groups (OH) of EVOH polymer chains, sulfone groups (-SO$_2$) of PSF polymer bulk chains and hydrophilic HNTs reduced HNT agglomeration thus enhancing MMM modification efficiency. The resulting casting solution demonstrated high stability. In addition, MD simulations and Raman analyses showed the presence of H-bonding interactions between PSF, EVOH, PEG, and HNTs, which was responsible for the stable and uniform distribution of HNTs in the PSF/EVOH base polymer matrix. Multiple hydrogen bonds were formed because of the intrinsic increase in the concentration of the HNT, which resulted in thermodynamically stable solutions with high viscosity and delayed demixing. As a result, asymmetric MMMs with a spongy structure with no reduction in permeance were formed. Results of the ultrasonic transmission experiments corresponded well with the thermodynamic and membrane morphology data. Furthermore, during the mutual diffusion process, the surface segregation behavior of the HNTs with SiO, AlOH, and hydroxyl (OH) groups, as well as PSF with (-SO$_2$)- and EVOH-terminal hydroxyl (OH) groups, promoted the migration of the hydrophilic groups to the surface of the MMMs. This increased

hydrophilicity resulted in the PSF/EVOH/HNTs-MMM with high water permeance. The membrane permeance of PSF/EVOH-HNTs increased from 246 L m^{-2}h^{-1} bar-1 for the M0 pristine membranes to 419 L m^{-2}h^{-1} bar^{-1} for the M12 MMM with the HNTs concentration of 0.12. wt.%. This enhancement in permeance can be attributed to an increase in the surface hydrophilicity of the pore structure, size, and porosity of the PSF/EVOH/HNTs membrane. The inclusion of HNTs fillers also improved tensile strength and elongation at break. In addition, the MMMs (M12) showed higher antifouling performance (PRR of 97.8% for BSA and 93.8% for oil) compared to (PRR of 83.5% for BSA and 76.5% for oil) M0. By demonstrating the synergy between the base polymers PSF/EVOH and the HNT nanoparticles, this study paves the way for the development of high-performance UF membranes without macrovoids.

Declarations

Author contributions

Sania Kadanyo: Conceptualization, Formal analysis, Investigation, Writing - original draft, Writing - review & editing.

Christine N. Matindi: Investigation, Writing - Review and editing.

Nozipho N. Gumbi: Investigation, Writing - Review and editing. **Derrick S. Dlamini:** Writing - Review and editing. **Yunxia Hu:** Investigation. **Zhenyu Cui:** Writing - review & editing. **Benqiao He** Investigation. **Bhekie B. Mamba** and **Jianxin Li:** Conceptualization, Funding acquisition, Writing - Review & editing, Supervision.

Corresponding authors

Correspondence to J.L or B.B.M

Data availability

The authors declare that all further data supporting the study's conclusions are included in the publication and its supplemental material files.

Competing Interests

The authors declare no competing interests.

References

1. Ercin, A. E. & Hoekstra, A. Y. Water footprint scenarios for 2050: A global analysis. Environ. Int. **64**, 71–82 (2014).

2. Issaoui, M., Jellali, S., Zorpas, A. A. & Dutournie, P. Membrane technology for sustainable water resources management: Challenges and future projections. Sustain. Chem. Pharm. **25**, 100590 (2022).

3. Zhu, Y., Wang, D., Jiang, L. & Jin, J. Recent progress in developing advanced membranes for emulsified oil/water separation. NPG Asia Materials. **6**, 11 (2014).

4. Guillen, G. R., Pan, Y., Li, M. & Hoek, E. M. V. Preparation and characterization of membranes formed by nonsolvent induced phase separation: A review. Ind. Eng. Chem. Res. **50**, 3798–3817 (2011).

5. Hilal, N. & Wright, C. J. Exploring the current state of play for cost-effective water treatment by membranes. NPJ Clean Water. **1**,1–4 (2018).

6. Li, S., Cui, Z., Zhang, L., He, B. & Li, J. The effect of sulfonated polysulfone on the compatibility and structure of polyethersulfone-based blend membranes. J. Membr. Sci. **513**, 1–11 (2016).

7. Wen, X., He, C., Hai, Y., Ma, R., Sun, J., Yang, X., Qi, Y., Wei, H. & Chen, J. Fabrication of an antifouling PES ultrafiltration membrane via blending SPSF. RSC Adv. **12**, 1460–1470 (2022).

8. Awad, E. S., Sabirova, T. M., Tretyakova, N. A., Alsalhy, Q. F., Figoli, A., & Salih, I. K. A Mini-Review of Enhancing Ultrafiltration Membranes (UF) for Wastewater Treatment: Performance and Stability. Chem. Eng. J. **5**, 34 (2021).

9. Bairamov, D. F., Chalykh, A. E., Feldstein, M. M. & Siegel, R. A. Impact of Molecular Weight on Miscibility and Interdiffusion between Poly (N-vinyl pyrrolidone) and Poly(ethylene glycol). Chem. Phys. **203**, 2674–2685(2002).

10. Kadanyo, S., Gumbi, N. N., Matindi, C. N., Dlamini, D. S., Hu, Y., Cui, Z., Wang, H., Hu, M. & Li, J. Enhancing compatibility and hydrophilicity of polysulfone/poly (ethylene-co-vinyl alcohol) copolymer blend ultrafiltration membranes using polyethylene glycol as hydrophilic additive and compatibilizer. Sep. Purif. Technol. **287**, 120523 (2022).

11. Miao, R., Wang, L., Gao, Z., Mi, N., Liu, T., Lv, Y., & Wang, X. Polyvinylidene fluoride/poly (ethylene-co-vinyl alcohol) blended membranes and a systematic insight into their antifouling properties. RSC Adv. **5**, 36325–36333 (2015).

12. Zhu, K., Zhang, S., Luan, J., Mu, Y., Du, Y., & Wang, G. Fabrication of ultrafiltration membranes with enhanced antifouling capability and stable mechanical properties via the strategies of blending and crosslinking. J. Membr. Sci. **539**, 116–127 (2017).

13. Fang, L. F., Yang, H. Y., Cheng, L., Kato, N., Jeon, S., Takagi, R., & Matsuyama, H. Effect of molecular weight of sulfonated poly (ether sulfone) (SPES) on the mechanical strength and antifouling properties of poly (ether sulfone)/SPES blend membranes. Ind. Eng. Chem. Res. **56**, 11302–11311 (2017).

14. Zhang, L., Cui, Z., Hu, M., Mo, Y., Li, S., He, B., & Li, J. Preparation of PES/SPSf blend ultrafiltration membranes with high performance via H2O-induced gelation phase separation. J. Membr. Sci. **540**, 136–145 (2017).

15. Ren, J., Zhang, S., Liu, Y., Wang, Y., Pang, J., Wang, Q., & Wang, G. A novel crosslinking organic-inorganic hybrid proton exchange membrane based on sulfonated poly (arylene ether sulfone) with 4-amino-phenyl pendant group for fuel cell application. J. Membr. Sci. **434**, 161–170 (2013).

16. Luo, L., Chung, T. S., Weber, M., Staudt, C. & Maletzko, C. Molecular interaction between acidic sPPSU and basic HPEI polymers and its effects on membrane formation for ultrafiltration. J. Membr. Sci. **524**, 33–42 (2017).

17. Noamani, S., Niroomand, S., Rastgar, M. & Sadrzadeh, M. Carbon-based polymer nanocomposite membranes for oily wastewater treatment. NPJ Clean Water. **2**, 1–4 (2019).

18. Alvarez, P. J. J., Chan, C. K., Elimelech, M., Halas, N. J. & Villagrán, D. Emerging opportunities for nanotechnology to enhance water security. Nat. Nanotechnol. **13**, 634–641 (2018).

19. Grylewicz, A. & Mozia, S. Polymeric mixed-matrix membranes modified with halloysite nanotubes for water and wastewater treatment: A review. Sep. Purif. Technol. **256**, 117827 (2021).

20. Keskin, B., Ağtaş, M., Ormancı-Acar, T., Türken, T., İmer, D.Y., Ünal, S., Menceloğlu, Y.Z., Uçar-Demir, T. & Koyuncu, İ. Halloysite nanotube blended nanocomposite ultrafiltration membranes for reactive dye removal. Water Sci. Technol. **83**, 271–283 (2021).

21. Kamal, N., Ahzi, S. & Kochkodan, V. Polysulfone/halloysite composite membranes with low fouling properties and enhanced compaction resistance. Appl. Clay Sci. **199**, 105873 (2020).

22. Makaremi, M., de Silva, R. T. & Pasbakhsh, P. Electrospun nanofibrous membranes of polyacrylonitrile/halloysite with superior water filtration ability.J. Phys. Chem. C. **119**, 7949–7958 (2015).

23. Mozia, S., Grylewicz, A., Zgrzebnicki, M., Darowna, D. & Czyzewski, A. Investigations on the properties and performance of mixed-matrix polyethersulfone membranes modified with halloysite nanotubes. Polymers (Basel). **11**, 671 (2019).

24. Chu, Z., Chen, K., Xiao, C., Ling, H. & Hu, Z. Performance improvement of polyethersulfone ultrafiltration membrane containing variform inorganic nano-additives. Polymer (Guildf.). **188**, 122160 (2020).

25. Buruga, K., Kalathi, J. T., Kim, K. H., Ok, Y. S. & Danil, B. Polystyrene-halloysite nano tube membranes for water purification. Ind. Eng. Chem. Res. **61**, 169–180 (2018).

26. Mishra, G. & Mukhopadhyay, M. Enhanced antifouling performance of halloysite nanotubes (HNTs) blended poly (vinyl chloride) (PVC/HNTs) ultrafiltration membranes: For water treatment. Ind. Eng. Chem. Res. **63**, 366–379 (2018).

27. Zhou, Z., Fang, L., Cao, Y., Wang, W., Wang, J., Yang, Y., & Liu, Y. Determination of Hansen solubility parameters of halloysite nanotubes and prediction of its compatibility with polyethylene oxide. Colloids Surf, A Physicochem Eng Asp. **601**, 125031 (2020).

28. Gumbi, N. N., Hu, M., Mamba, B. B., Li, J. & Nxumalo, E. N. Macrovoid-free PES/SPSf/O-MWCNT ultrafiltration membranes with improved mechanical strength, antifouling and antibacterial properties. J. Membr. Sci. **566**, 288–300 (2018).

29. Kar, F., and N. Arslan. Effect of temperature and concentration on viscosity of orange peel pectin solutions and intrinsic viscosity–molecular weight relationship. Carbohydr. Polym. **40**, 277–284 (1999).

30. Kuo, S. W, Hydrogen Bonding in Polymeric Materials, John Wiley & Sons (2018).

31. Kruglikov, A., Vasilchenko, A., Kasprzhitskii, A. & Lazorenko, G. Atomic-level understanding of interface interactions in a halloysite nanotubes-PLA nanocomposite. RSC Adv. **9**, 39505–39514 (2019).

32. Cai, Y., Li, J., Guo, Y., Cui, Z. & Zhang, Y. In-situ monitoring of asymmetric poly (ethylene-co-vinyl alcohol) membrane formation via a phase inversion process by an ultrasonic through-transmission technique. Desalination. **283**, 25–30 (2011).

33. Liu, S., Zhang, M., Huang, B., Wu, N. & Ouyang, S. Raman spectroscopy for the competition of hydrogen bonds in ternary (H_2O-THF-DMSO) aqueous solutions. Molecules. **24**, 3666 (2019).

34. Gilbert, A. S. Hydrogen Bonding and Other Physicochemical Interactions Studied by IR and Raman Spectroscopy. 957–962 (1999).

35. Fan, X., Su, Y., Zhao, X., Li, Y., Zhang, R., Ma, T., & Jiang, Z. Manipulating the segregation behavior of polyethylene glycol by hydrogen bonding interaction to endow ultrafiltration membranes with enhanced antifouling performance. J. Membr. Sci. **499**, 56–64 (2016).

36. Liu, Z., Mi, Z., Jin, S., Wang, C., Wang, D., Zhao, X., & Chen, C. The influence of sulfonated hyperbranched polyethersulfone-modified halloysite nanotubes on the compatibility and water separation performance of polyethersulfone hybrid ultrafiltration membranes. J. Membr. Sci. **557**, 13–23 (2018).

37. Zhang, L., Cheng, L., Wu, H., Yoshioka, T. & Matsuyama, H. One-step fabrication of robust and anti-oil-fouling aliphatic polyketone composite membranes for sustainable and efficient filtration of oil-in-water emulsions. J. Mater. Chem. **6**, 24641–24650 (2018).

38. Amid, M., Nabian, N. & Delavar, M. Performance evaluation and modeling study of PC blended membranes incorporated with SDS-modified and unmodified halloysite nanotubes in the separation of oil from water. J. Environ. Chem. Eng. **9**, 105237(2021).

39. Cui, Z., Tang, X., Li, W., Liu, H., Zhang, J., Wang, H., & Li, J. EVOH in situ fibrillation and its effect of strengthening, toughening and hydrophilic modification on PVDF hollow fiber microfiltration membrane via TIPS process. J. Membr. Sci. **54**, 5971–5987 (2019).

40. Vatanpour, V., Madaeni, S. S., Khataee, A. R., Salehi, E., Zinadini, S., & Monfared, H. A. TiO_2 embedded mixed matrix PES nanocomposite membranes: Influence of different sizes and types of nanoparticles on antifouling and performance. Desalination. **292**, 19–29 (2012).

41. Amid, M., Nabian, N. & Delavar, M. Fabrication of polycarbonate ultrafiltration mixed matrix membranes including modified halloysite nanotubes and graphene oxide nanosheets for olive

oil/water emulsion separation. Sep. Purif. Technol. **251**, 117332. (2020).

42. Emadzadeh, D., Lau, W. J., Matsuura, T., Rahbari-Sisakht, M. & Ismail, A. F. A novel thin film composite forward osmosis membrane prepared from PSf-TiO2 nanocomposite substrate for water desalination. Chem. Eng. J. **237**, 70–80 (2014).

43. Wan Ikhsan, S. N., Yusof, N., Aziz, F. & Fauzi Ismail, A. Facile synthesis and characterization of Zno-HNT additive for enhancement of polysulfone membrane for Oil-In-Water separation. Mater. Today. **46**, 1978–1982 (2020).

44. Yuan, S., Zhu, J., Li, Y., Zhao, Y., Li, J., Van Puyvelde, P., & Van der Bruggen, B. Structure architecture of micro/nanoscale ZIF-L on a 3D printed membrane for a superhydrophobic and underwater superoleophobic surface. J. Mater. Chem. A. **7**, 2723–2729 (2019).

45. Han, M. J., Baroña, G. N. B. & Jung, B. Effect of surface charge on hydrophilically modified poly (vinylidene fluoride) membrane for microfiltration. Desalination 270, 76–83 (2011).

46. Flemming, H.-C. & Schaule, G. Biofouling on membranes-a microbiological approach. Desalination. **70**, 95–119 (1988).

47. Lin, A. G., Zhang, G. Z. & Liu, G. Electrokinetic phenomena of modified polytetrafluoroethylene membranes in oily sewage from oil field.J. Chem. Pet. Eng. **23**, 66–69 (2007).

48. Ravichandran, G., Rathnakar, G., Santhosh, N., Chennakeshava, R. & Hashmi, M. A. Enhancement of mechanical properties of epoxy/halloysite nanotube (HNT) nanocomposites. Appl. Sci. **1**, 1–8 (2019).

49. Li, X., Nayak, K., Stamm, M. & Tripathi, B. P. Zwitterionic silica nanogel-modified polysulfone nanoporous membranes formed by in-situ method for water treatment. Chemosphere. **280**, 130615 (2021).

50. Mu, K. Mu, K., Zhang, D., Shao, Z., Qin, D., Wang, Y., & Wang, S. Enhanced permeability and antifouling performance of cellulose acetate ultrafiltration membrane assisted by L-DOPA functionalized halloysite nanotubes. Carbohydr. Polym. **174**, 688–696 (2017).

Scheme

Schemes 1 and 3-5 are available in Supplementary Files section.

Tables

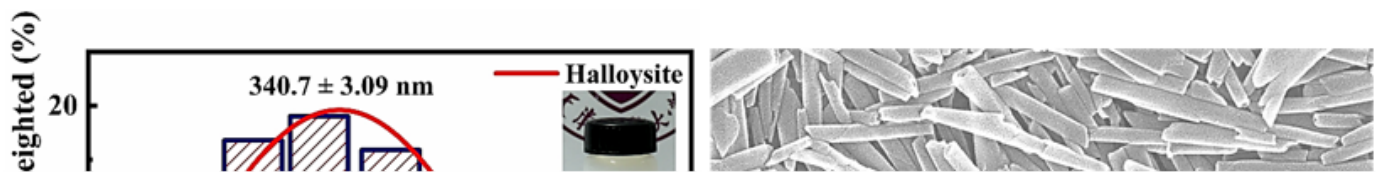Table 3 is not available with this version

Figures

Figure 1

(a) DLS Histogram of length distribution of HNTs; (b) SEM photographs of the examined HNTs (c) TEM-EDX elemental distribution of the examined HNTs.

Figure 2

Digital photos of PSF/EVOH32/PEG/HNTs solutions with different storage times: (a) freshly-prepared samples; (b) samples stored for 4 weeks at 25 °C; and (c) samples stored for 4 at weeks at 25 °C and thereafter reheated to 70 °C.
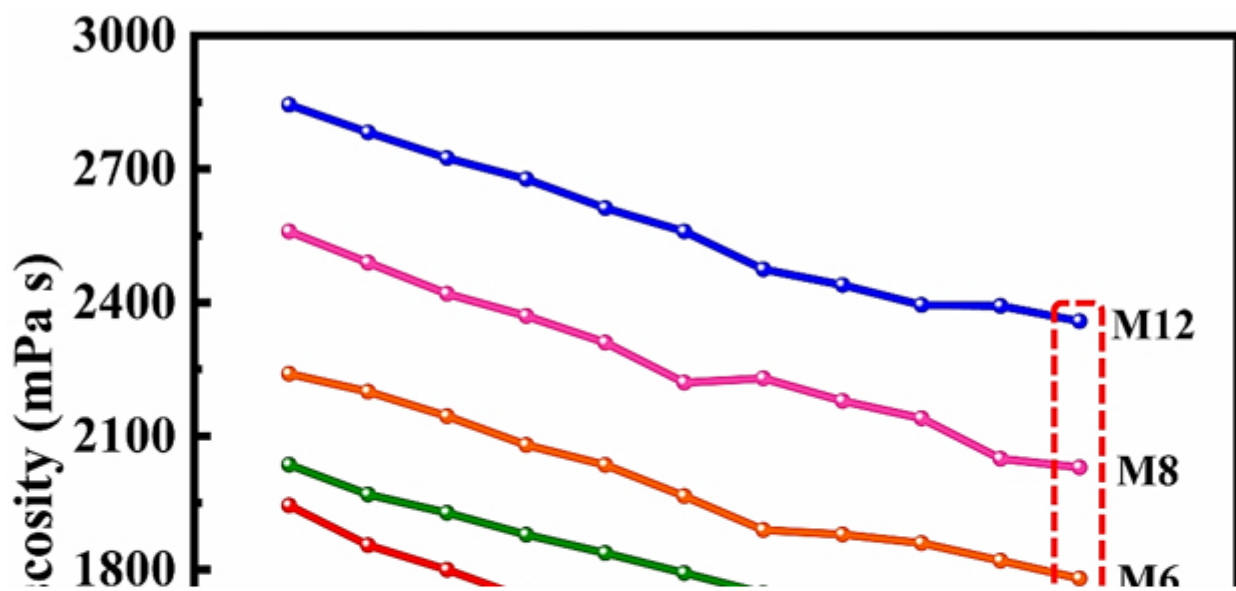
Figure 3

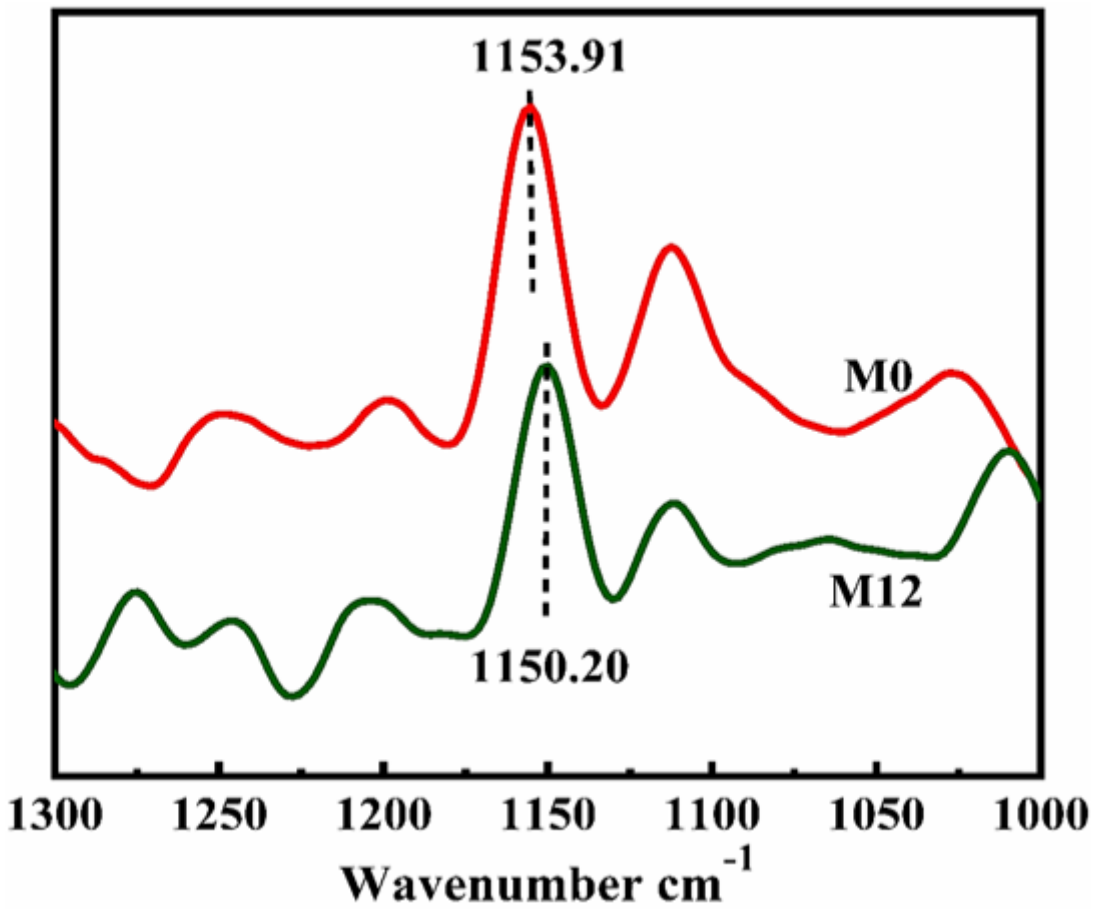*Viscosity curves of PSF/EVOH (20 wt. %) casting solution with increasing HNT content and temperature*

Figure 4

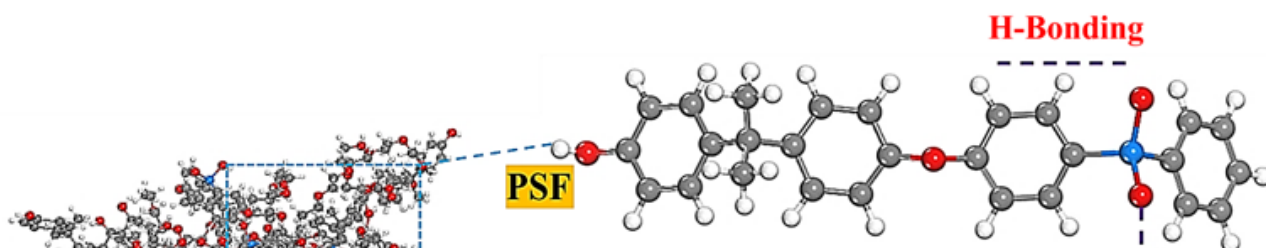Raman spectra of PSF/EVOH (M0) and PSF/EVOH /HNT (M12) casting solutions

Figure 5

(a) The amorphous structure of the PSF/EVOH/PEG/HNT system, with the magnified section on the right exhibiting H-bonding interaction between PSF and HNT, EVOH and HNTs, and PEG and HNT. C: black, H: white, O: red, S: yellow; (b) RDF calculation of PSF and HNTs; EVOH and HNTs; and of PEG and HNTs.
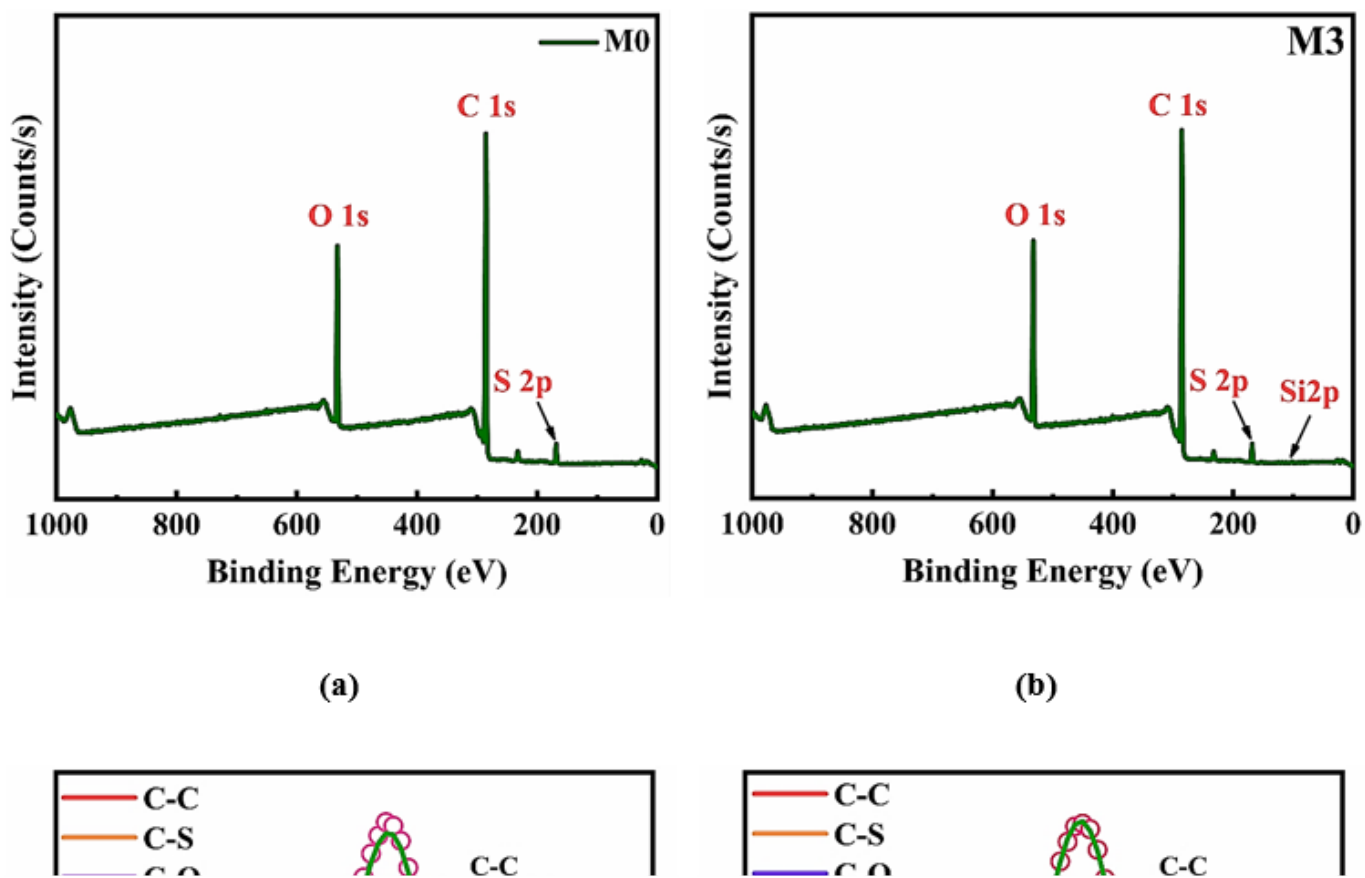
Figure 6

XPS spectra for M0 (a) and M3 (b) and deconvoluted peaks for M0 (c) and M3 (d).

Figure 7

SEM images of MMMs: (a,g) M0; (b) M2; (c) M3; (d,h) M6; (e) M8; (f) M12.

Figure 8

TEM micrographs showing distribution of HNTs in M6 (a) TEM micrographs (b) EDX mapping image of the PSF/EVOH/HNTs MMMs

Figure 9

Ultrasonic signal spectra during membrane formation (a) and ultrasonic signal movement in time-domain during the membrane formation (b).

Figure 10

The Air–Water stability dynamic water contact angle of the blend membranes (a) and oil–Water Contact Angles (b).

Figure 11

The surface zeta potential of the PSF/EVOH membrane and MMMs

Figure 12

The Mechanical strength of the PSF/EVOH membrane and MMMs.

Figure 13

Pure water permeance (PWP) (a) and solute permeance (SP) of the membranes for the treatment of BSA and oil-in-water emulsion (gasoline) (b)

Figure 14

Permeance versus operating time of the PSF/EVOH blend membrane and PSF/EVOH/HNTs MMMs during the fouling and cleaning operating process (phases I, III, V, and VII: pure water filtration and II, IV, and VI: BSA permeation. Each phase was run for 60 min) (a) and permeance recovery rate (PRR) of blend membranes for the treatment of BSA and oil-in-water emulsion

Supplementary Files

This is a list of supplementary files associated with this preprint. Click to download.

- SuportingdocumentKadanyoetalXL.docx
- GA1.png
- Scheme1.png
- Scheme3.png
- Scheme4.png
- Scheme5.png